

The kinematics of molecular clumps surrounding hot cores in G29.96−0.02 and G31.41+0.31

C. Maxia^{1,2}, L. Testi³, R. Cesaroni³, and C.M. Walmsley³

¹ Osservatorio Astronomico di Cagliari, Str. 54, Loc. Poggio dei Pini, I-09012 Capoterra (CA), Italy

² Dipartimento di Scienze Fisiche, Università di Cagliari, Cittadella Universitaria, I-09042 Monserrato (CA), Italy

³ Osservatorio Astrofisico di Arcetri, Largo E. Fermi 5, I-50125 Firenze, Italy

Received 29 December 2000/Accepted 15 February 2001

Abstract. We present high angular resolution interferometric observations of the 3 and 1.3 mm continuum emission, and HCO⁺(1–0) and SiO(2–1) $v=0$ lines, obtained with the Owens Valley Radio Observatory millimeter-wave array, toward two hot cores (HCs) associated with two well known ultracompact (UC) H II regions: G29.96−0.02 and G31.41+0.31. These HCs are believed to host young forming massive stars which have been suggested to be surrounded by massive rotating accretion disks. The aim of these new observations is to study the structure and kinematics of the molecular clumps surrounding the HCs and nearby UC H II regions at moderately high angular resolution. Our observations reveal that the clumps within which the HCs and UC H II regions are embedded have a complex kinematical structure. The total mass of the clumps is estimated to be in the range 1000–3000 M_{\odot} , consistent with previous findings. Our observations also show compelling evidence that the clump in G29.96−0.02 is contracting onto the HC position, suggesting that the accretion process onto the massive young stellar object embedded in the HC is still ongoing. In these objects the kinematical structure that we observe is also compatible with the presence of a massive rotating disk within the HC, even though we cannot prove this suggestion with our data. The case of G31.41+0.31 is more complicated, and our data, although consistent with the presence of an inner disk and an infalling envelope around it, do not have the required spatial resolution to resolve the different structures.

Key words. ISM: clouds – H II regions – ISM: individual objects: G29.96−0.02, G31.41+0.31 – ISM: molecules – Radio lines: ISM

1. Introduction

The importance of the study of high-mass star formation derives from the close interaction between such stars and the interstellar medium: they affect the ISM evolution and, consequently, the galactic evolution in general. In spite of this, until the last few years the study of star formation was mostly concentrated on low-mass stars, because of the difficulties in investigating young massive stars, less numerous, more distant, more embedded and with much shorter evolutionary timescales. The search for the sites where the first phases of high-mass star formation occurs has been increasing recently, because of the advent of aperture synthesis mm-interferometers (Kurtz et al. 2000).

High-mass stars ignite hydrogen burning and reach the main sequence while still accreting matter (Palla & Stahler 1993). Thus young massive stars are still deeply embedded in a dense gas and dust envelope which impairs the detection at optical and near infrared wavelengths.

Due to the large luminosity and Lyman photon emission, a newly born massive star heats the dust and ionises the gas in the surrounding envelope and can be detected in the far-infrared (FIR) as a luminous IRAS source and in the centimetric radio continuum as an ultracompact (UC) H II region (Wood & Churchwell 1989a; 1989b). However, these are signposts of already-formed massive stars; in order to study the more elusive evolutionary phase of main accretion one has to devise suitable target selection procedures. Several different approaches have been explored to obtain lists of candidate massive accreting protostars (see the review by Kurtz et al. 2000): high-luminosity IRAS sources with peculiar colours (e.g. Molinari et al. 1996; 1998), H₂O masers without associated radio continuum emission (Tofani et al. 1995; Cesaroni et al. 1999b), compact molecular cores close to UC H II regions (Cesaroni et al. 1991; 1994a). The latter approach is supported by the observational result that massive stars are usually found in rich clusters and associations: it is thus likely to find a forming massive star lying close to a young one. In this way Cesaroni et al. (1994a) identified com-

compact molecular cores close to, but generally not coincident with, the target UC H II regions. These are characterized by bolometric luminosities exceeding $10^4 L_{\odot}$, small diameters (≤ 0.1 pc) and kinetic temperatures over 50 K, and were then called hot cores (HCs). Due to their high luminosity and temperature, HCs have been suggested to contain very young massive (proto-)stars. In fact, a few of them contain UC H II regions (e.g. G10.47+0.03, see Cesaroni et al. 1998), which witness the existence of embedded early type stars. Moreover, two well known HCs, IRAS 20126+4104 (Cesaroni et al. 1997; 1999a) and G9.62+0.19–F (Hofner et al. 1996b; Testi et al. 1998; 2000), show evidence of an embedded massive young stellar object in a phase preceding the formation of a classical UC H II.

Two of the best studied classical HCs from the list of Cesaroni et al. (1994a) are those close to the UC H II regions G29.96–0.02 and G31.41+0.31. In the former region the molecular core lies in front of the cometary UC H II region, approximately $2''.6$ west of the 1.3 cm continuum peak. In G31.41+0.31, faint NH_3 emission is detected toward the extended halo around the UC H II region, while the NH_3 HC peak is $\sim 4''$ to the southwest of the centimetric radio continuum peak. High angular resolution ($\sim 0.4''$) Very Large Array (VLA) observations of the $\text{NH}_3(4,4)$ inversion transition (Cesaroni et al. 1998) showed resolved emission from both HCs, with a deconvolved size of $\sim 1''.4$ in G29.96–0.02 and $\sim 1''.8$ in G31.41+0.31. Both cores appear slightly elongated: G29.96–0.02 in the E–W direction and G31.41+0.31 along a SW–NE axis. A velocity gradient of approximately $2\text{--}3 \text{ km s}^{-1} \text{ arcsec}^{-1}$ over $3''$ is found along such directions. Similar correlations are found in the $\text{CH}_3\text{CN}(6\text{--}5)$ transition for both G29.96–0.02 and G31.41+0.31, although the velocity gradients in CH_3CN ($\sim 15 \text{ km s}^{-1} \text{ arcsec}^{-1}$) are larger than those observed in NH_3 (Cesaroni et al. 1994b; Hofner et al. in prep.). Also, in both sources the derived kinetic temperature shows a peak toward the center. All these features have been interpreted as evidence of disk-like structures rotating about a hot, massive central object: the (proto-)star.

The presence of a deeply embedded massive (proto-)star is also indirectly suggested by the presence of several other signposts, such as H_2O and H_2CO , CH_3OH masers toward the hot ammonia core peak of G29.96–0.02 (Hofner & Churchwell 1996a; Pratap et al 1994; Walsh et al. 1998) and H_2O masers toward G31.41+0.31 (Gaume & Mutel 1987).

Recently, Pratap et al. (1999) investigated the molecular gas surrounding G29.96–0.02 using the BIMA millimeter wave interferometer with moderate angular resolution ($\sim 10''$). They found ^{13}CO and high-density tracer (CS and CH_3CN) emission; while the former molecule is found in an extended cloud surrounding both the HC and the UC H II, the latter peak toward the HC position. Hence, CH_3CN and NH_3 emission trace the innermost and warmer molecular gas within the HC itself, while ^{13}CO traces the large-scale molecular cloud in which the HC, the UC H II region and the surrounding near infrared

young stellar cluster are embedded. Pratap et al. (1999) also detected a compact core of CH_3OH emission, $\sim 5''$ south west of the HC. This second core does not show the typical features of HCs (compact NH_3 and CH_3CN emission) and Pratap et al. suggest that it may be associated with a molecular outflow from the HC exciting source or with a low-mass star forming outside it.

In order to study the relationship between the HC and the UC H II region, and the kinematics of the gaseous clump in which these are embedded, we decided to obtain high angular resolution observations of the $\text{HCO}^+(1\text{--}0)$ and $\text{SiO}(2\text{--}1) v=0$ lines, as already done in similar regions by other authors (Acord, Walmsley & Churchwell 1997; Cesaroni et al. 1997; Wilner et al. 1996). These tracers are expected to provide information on the innermost part of the cloud and the kinematics of the molecular gas at the interface between the HC and the UC H II region. The main goal of the observations was thus to relate the observed velocity field within the HC to the kinematics of the molecular gas in the inner portions of the cloud. Additionally, the $\text{SiO}(2\text{--}1) v=0$ transition, which can be enhanced in shocked regions, was expected to clarify the CH_3OH observations of Pratap et al. (1999).

Throughout this paper we will assume a distance of 6 kpc for G29.96–0.02, based on the recent estimate of Pratap et al. (1999), and 7.9 kpc for G31.41+0.31, based on the kinematic estimate of Churchwell et al. (1990).

We present our new millimeter interferometric observations and data reduction in Sect. 2. In Sect. 3 the observational results are presented for the millimeter continuum and molecular lines separately. We discuss the implications of our results on the structure of the two regions and the nature of HCs in Sect. 4. In Sect. 5 we summarize the main results of our study.

2. Observations and data reduction

High resolution interferometric observations were performed in the period October–December 1997 using the Owens Valley Radio Observatory (OVRO) millimeter-wave array, located near Big Pine, California. The array comprises six 10.4 m dishes that were employed in three different configurations yielding baselines in the range 15–220 m. The phase centers used were: $\alpha_{1950} = 18^{\text{h}}43^{\text{m}}27^{\text{s}}.1$, $\delta_{1950} = -02^{\circ}42'36''.4$ for G29.96–0.02 and $\alpha_{1950} = 18^{\text{h}}44^{\text{m}}59^{\text{s}}.1$, $\delta_{1950} = -01^{\circ}16'07''.3$ for G31.41+0.31. The half-power beamwidth of the OVRO antennas is $\sim 84''$ at 88 GHz, and $\sim 32''$ at 233 GHz. Each antenna is equipped with cryogenically cooled SIS receivers that offered typical system temperatures of ~ 300 K at 88 GHz, and ~ 1200 K at 233 GHz. The 3.4 mm and 1.3 mm continuum observations employed an analog correlator for a total bandwidth, at each of the two frequencies, of ~ 2 GHz. The flexible digital correlator was configured to observe simultaneously the $\text{HCO}^+(1\text{--}0)$ and $\text{SiO}(2\text{--}1) v=0$ transitions at 89.2 and 86.8 GHz respectively. For both molecules we used a $\sim 105 \text{ km/s}$ wide band with $\sim 1.7 \text{ km/s}$ resolution.

The spectrometer modules were centered at ~ 98 km/s, close to the systemic velocity of both sources.

Complex gain calibration was ensured by frequent observations of 1741–038. The typical observing cycle alternated scans on G29.96–0.02, G31.41+0.31 and 1741–038 with a period of ~ 30 min. 3C273 was used as passband calibrator and Uranus and/or Neptune were used to set the flux scale. The expected flux calibration uncertainty is $\sim 20\%$. Data calibration and editing has been performed using the MMA software package (Scoville et al. 1993). At 230 GHz data could be salvaged only for a small subset of the observations, due to the poor phase stability and relatively high water vapour content of the atmosphere during most of the observations. This resulted in a poor (u, v) coverage of the final 233 GHz dataset, a final noise higher than normally expected and a much reduced sensitivity to the extended structures. The calibrated (u, v) datasets were exported to the NRAO–AIPS package for imaging and analysis. All the maps presented in this paper were obtained with the AIPS IMAGR task using natural weighting of the (u, v) data.

In the continuum maps, the final synthesised half power beam width (HPBW) is $5''.9 \times 3''.7$, with P.A. ~ -8 , at 88 GHz, and $4''.9 \times 2''.7$, with P.A. ~ -3.5 , at 233 GHz, for both sources. The rms level is 10 mJy/beam at 88 GHz for both sources, 40 mJy/beam for G29.96–0.02 and 160 mJy/beam for G31.41+0.31 at 233 GHz. In the line cubes we obtained $5''.9 \times 3''.7$ HPBW and 50 mJy/beam rms level for all lines. The P.A. is -10.5 for the HCO^+ and -16.1 for the SiO for G29.96–0.02; -9.2 for the HCO^+ and -14.9 for the SiO line for G31.41+0.31. The conversion factor from flux density to brightness temperature in the synthesised beam is ~ 10.4 K $(\text{Jy/beam})^{-1}$ at 88 GHz and ~ 2.43 K $(\text{Jy/beam})^{-1}$ at 233 GHz.

2.1. Continuum maps

Our millimeter continuum maps are sensitive to both the free-free emission from the ionised gas inside the UC H II regions and the thermal dust emission. The latter is mainly confined to the HC region (Olmí et al. 1996; Patrap et al. 1999). In order to disentangle the HC continuum emission from that of the UC H II region, we need to estimate the contribution of the free-free emission at millimeter wavelengths and subtract it from our continuum maps. To this purpose we have used the 24 GHz VLA observations of Cesaroni et al. (1994a; 1998). We re-imaged the calibrated (u, v) data using the same (u, v) range and restoring beam as the 88 and 233 GHz OVRO observations. These maps were then scaled assuming optically thin free-free emission ($F_\nu \propto \nu^{-0.1}$). In Figs. 1 and 2, we show for each source and each frequency the millimeter continuum maps as observed at OVRO (top panels), the free-free emission maps obtained by extrapolation of the VLA data (central panels), and the residual “dust” emission maps after removal of the free-free emission from the millimeter observations (bottom panels).

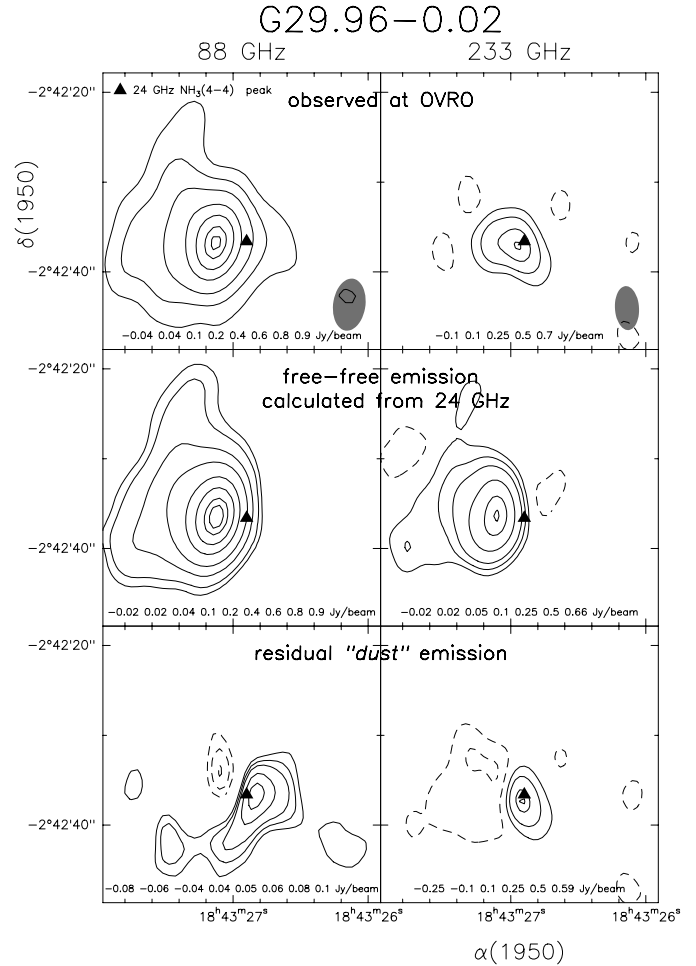


Fig. 1. Top panels: 88 and 233 GHz millimeter continuum maps observed at OVRO towards G29.96–0.02. Central panels: expected free-free contribution computed from the 24 GHz VLA data of Cesaroni et al. (1994a; 1998) using the same (u, v) range and restoring beam as in the top panels. Bottom panels: residual “dust emission” maps after subtracting the central panels from the top panels maps. The filled triangle marks the ammonia HC peak position. The beamsize at each frequency is shown on the top panels.

Figures 1 and 2 show that the procedure described above allowed us to compute a fairly accurate estimated map of the free-free emission contribution at millimeter wavelengths. The subtraction of the extended UC H II is successful in all cases except for the 233 GHz observations of G29.96–0.02. In this case, the poor (u, v) coverage of the millimeter map does not allow a proper reconstruction of the extended emission, and even if the free-free map was calculated using the same (u, v) range as the millimeter map, the much finer VLA sampling of the (u, v) plane allowed us to properly map part of the extended emission. When the subtraction of the calculated map is performed, the free-free emission from the UC H II is over-subtracted, producing a large negative hole at the position of the UC H II. On the other hand, also in this case, the

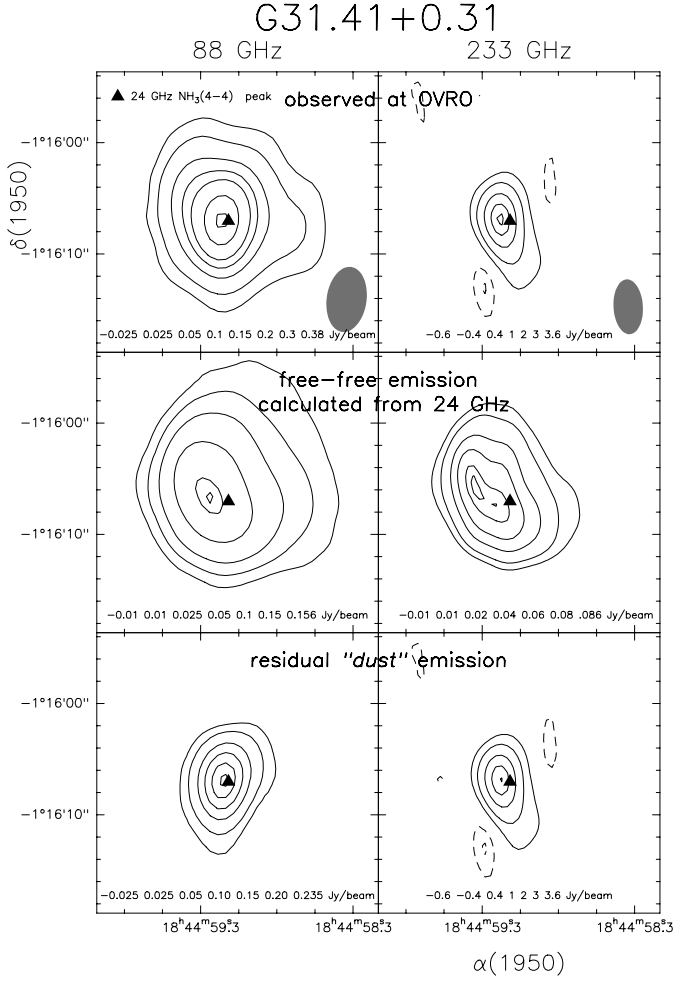


Fig. 2. As in Fig. 1, for G31.41+0.31.

position of the excess “dust” emission at 233 GHz is coincident with the NH_3 core and the 88 GHz “dust” peak. Toward G31.41+0.31 the free-free contribution to the millimeter emission is lower: at 88 GHz, the observed continuum peak is twice the value calculated from the 1.3 cm map, whereas at 233 GHz the maximum of the expected free-free emission is less than the 1σ noise level in the observed continuum map. In this case, the observed flux at 233 GHz is essentially thermal dust emission. However, as for G29.96−0.02, the total continuum flux at 233 GHz measured in our interferometric maps is less (a factor of ~ 3 for G31.41+0.31) than what expected from previous single dish observations (see Fig. 3), probably due to the spatial filtering of extended emission (see also Sect. 3.1).

2.2. Line maps

Continuum subtraction from the line data cubes was performed both in the (u, v) plane using the AIPS task UVLIN, selecting line free channels prior to image deconvolution, and in the image plane after cleaning, by subtracting the appropriate continuum images. The two techniques offered comparable results. The analysis pre-

Table 1. SED fit parameters

source	d (Kpc)	$r_{\text{H II}}$ (pc)	$T_{\text{H II}}$ (K)	$\log N_{\text{Ly}}$ (ph./s)	T_{dust} (K)	β
G29.96−0.02	6	0.5	6500	48.90	30	2
G31.41+0.31	7.9	0.5	8000	48.75	37	1

sented in this paper uses the continuum subtracted cubes produced with the second method.

3. Results

3.1. Continuum

In Fig. 3 we show the spectral energy distribution (SED) for G29.96−0.02 (top) and G31.41+0.31 (bottom). The flux density measurements that we used are a compilation of single dish and interferometer observations (see references in Fig. 3). The data are heterogeneous in both angular resolution and (u, v) coverage. The SED is that typical of UC H II regions, see also Wood & Churchwell (1989b), dominated by free-free emission at centimeter wavelengths and by thermal dust emission at millimeter and far-infrared wavelengths.

To give an estimate of global parameters, such as the supply rate of Lyman photons required to maintain the UC H II region ionised and the average temperature of the dust, we used a simplified two component model: a spherical and homogeneous H II region, plus a single temperature grey-body dust component. This simplified model is able to accurately reproduce the radio to far infrared portion of the SEDs shown in Fig. 3. In Table 1 we report the values of the fixed parameters of the models: distance (d) and electron temperature ($T_{\text{H II}}$) of the UC H II regions. For G29.96−0.02, we used the values estimated by Pratap et al. (1999); for G31.41+0.31, the distance is that estimated by Churchwell et al. (1990), whereas the temperature is a mean value for a typical H II region. Also shown in the table are the values of the parameters derived from our model fits: UC H II radius ($r_{\text{H II}}$), Lyman photons supply rate (N_{Ly}), dust temperature (T_d), and dust opacity index (β).

From the SEDs reported in Fig. 3, we can clearly see that our 233 GHz observations are well below both the single dish points and the model fits, especially in the case of G29.96−0.02, where the contribution of the UC H II free-free emission at such high frequency is still a consistent fraction of the total emission. This is mainly due to the sparse (u, v) coverage of our synthesis at this wavelength, and the inability to properly image extended structures. Hence, as discussed in Sect. 2.1, our 233 GHz observations cannot be used to infer the properties of the large scale structures in these regions, but offer only an estimate of the high frequency emission of the HCs themselves.

The values of T_{dust} and β are average values for the dust in the envelope surrounding the HCs, not the appro-

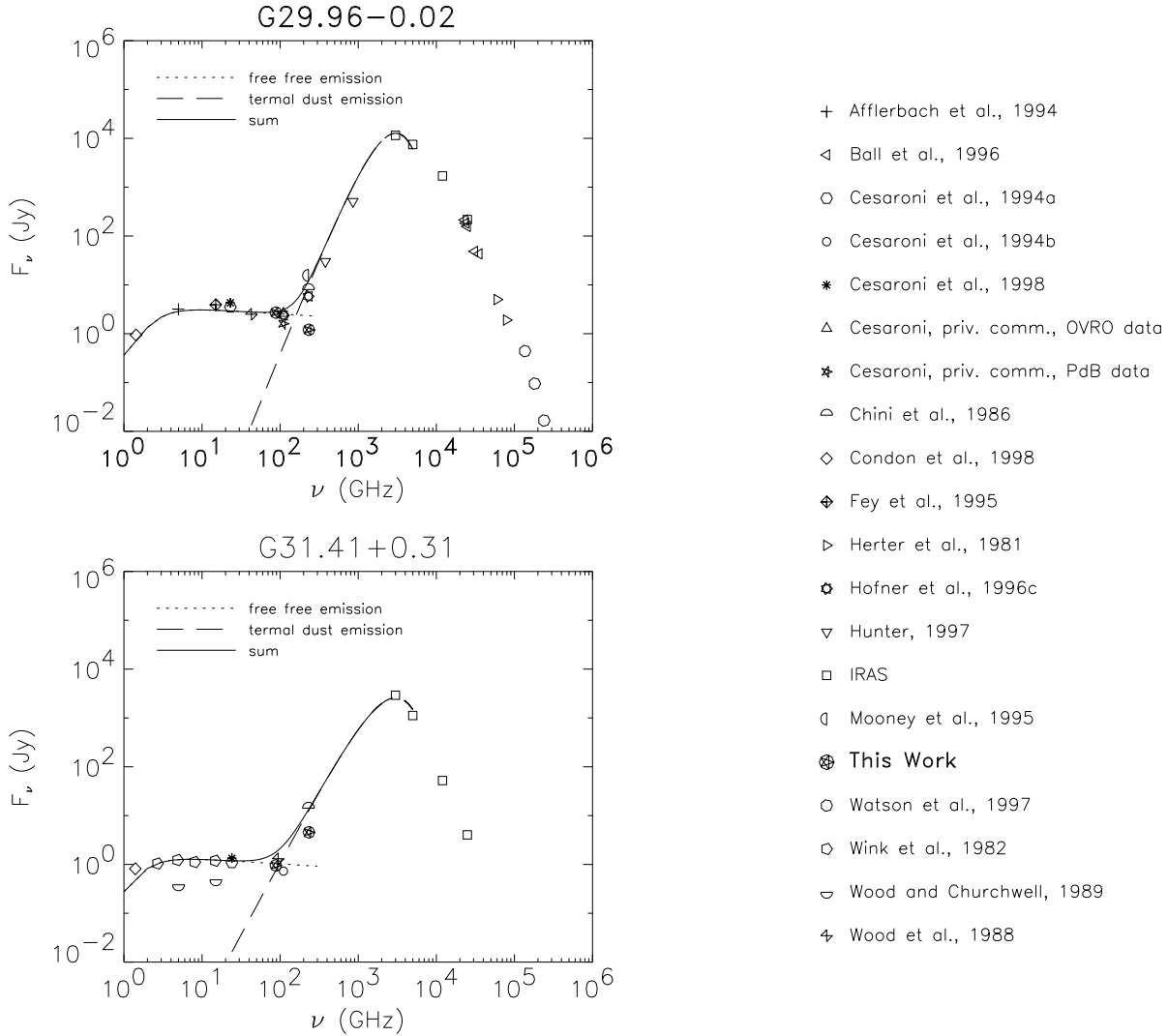


Fig. 3. Spectral energy distribution for G29.96−0.02 and G31.41+0.31. The solid lines are fits of the SED assuming a simplified two component model: free-free emission from a spherical, homogeneous and dust-free H II region (dotted line), and grey-body thermal dust emission (dashed line). On the right we indicate the reference for each of the measurement reported in the plots.

Table 2. Observed parameters of the continuum (dust and free-free) emission

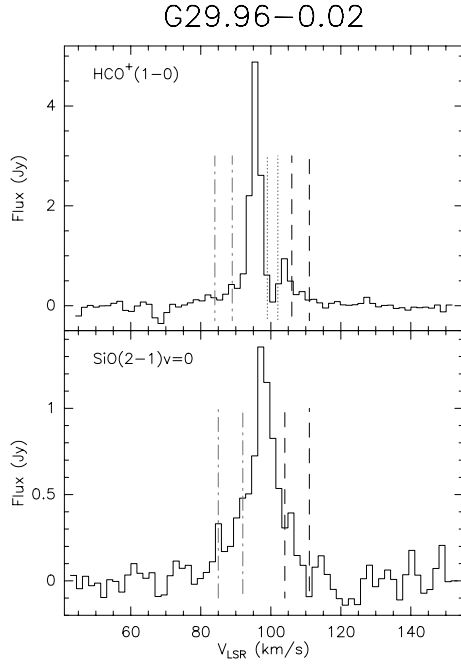
source	ν (GHz)	$\alpha_{1950}^{\text{peak}}$	$\delta_{1950}^{\text{peak}}$	F_ν^{peak} (Jy/beam)	F_ν (Jy)	$\Theta_{3\sigma}$ ($''$)	$\theta_{3\sigma}$ ($''$)	$r_{3\sigma}$ (pc)
G29.96−0.02	88	18:43:27.15	−2:42:37.1	0.92	2.7	20	20	0.28
	233	18:43:26.93	−2:42:36.9	0.71	1.2	8.1	6.9	0.10
G31.41+0.31	88	18:44:59.15	−1:16:07.3	0.39	0.92	16	15	0.28
	233	18:44:59.13	−1:16:06.8	3.7	4.2	7.1	5.7	0.11

priate values for the HCs since these will only contribute to a small fraction of the single dish submillimeter and far infrared fluxes. Nevertheless, the dust temperature that we derive is probably a good estimate of the kinetic temperature of the HCO⁺/SiO molecular clump surrounding the HC and UC H II region (see Sect. 3.2 below).

In Table 2, for each source and at each frequency, we report the peak position ($\alpha_{1950}^{\text{peak}}$ and $\delta_{1950}^{\text{peak}}$), the peak (F_ν^{peak}) and integrated fluxes (F_ν), the observed ($\Theta_{3\sigma}$) and deconvolved ($\theta_{3\sigma}$) angular diameter, and the corresponding linear radius ($r_{3\sigma}$) of the observed continuum emission (dust plus free-free, Figs. 1 and 2 top panels).

Table 3. Derived parameters of the dust continuum emission from the cores

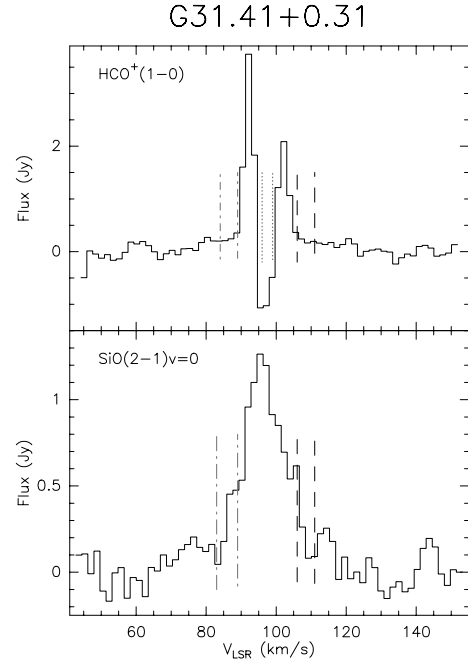
source	ν (GHz)	$\alpha_{1950}^{\text{peak}}$	$\delta_{1950}^{\text{peak}}$	F_{ν}^{peak} (Jy/beam)	F_{ν} (Jy)	$\Theta_{3\sigma}$ ($''$)	$\theta_{3\sigma}$ ($''$)	$r_{3\sigma}$ (pc)
G29.96−0.02	88	18:43:26.82	−2:42:36.4	0.11	0.24	11	9.5	0.14
	233	18:43:26.90	−2:42:37.4	0.60	0.56	5.8	4.0	0.06
G31.41+0.31	88	18:44:59.10	−1:16:06.6	0.24	0.28	9.5	7.8	0.15
	233	18:44:59.13	−1:16:06.8	3.6	4.0	6.9	5.5	0.10

**Fig. 4.** G29.96−0.02 source integrated spectra of the $\text{HCO}^+(1-0)$ and $\text{SiO}(2-1) v=0$ lines. The vertical lines indicate the velocity ranges used for the maps shown in Fig. 6 (see text for details).

In Table 3 the same quantities are reported for the estimated dust emission (Figs. 1 and 2 bottom panels). The observed angular diameters of the sources have been computed as $\Theta_{3\sigma} = 2\sqrt{A/\pi}$, where A is the area encompassing the observed source emission inside the 3σ contour level. The values of $\Theta_{3\sigma}$ have then been deconvolved using the expression $\theta_{3\sigma} = \sqrt{\Theta_{3\sigma}^2 - \Theta_B^2}$, where Θ_B is the synthesized HPBW. The linear radii have been calculated from $\theta_{3\sigma}$ using the adopted distances of 6 and 7.9 kpc, for G29.96−0.02 and G31.41+0.31 respectively (Pratap et al. 1999; Churchwell et al. 1990).

3.2. Line

In Figs. 4 and 5 we show the source integrated spectra for both $\text{HCO}^+(1-0)$ and $\text{SiO}(2-1) v=0$ transitions. The $\text{HCO}^+(1-0)$ spectra show absorption at a velocity very close to that of the ambient cloud in the case of G31.41+0.31, and redshifted in G29.96−0.02. No absorption is revealed in the $\text{SiO}(2-1) v=0$ spectra. From the

**Fig. 5.** As Fig. 4, for G31.41+0.31.

spectra, we selected the range of velocity channels highlighted by the vertical bars in Figs. 4 and 5, in order to produce maps of the HCO^+ absorption (dotted bars) and of the line wings (dashed for the red wings and dash-dotted bars for the blue wings). We produced also maps averaged over all the line emission.

The contour maps of the averaged $\text{HCO}^+(1-0)$ and $\text{SiO}(2-1) v=0$ emission, superimposed on the corresponding continuum in grey scale, are displayed in Fig. 6 for G29.96−0.02 and Fig. 7 for G31.41+0.31. The molecular emission in our HCO^+ and SiO maps of G29.96−0.02 is elongated toward the position of the CH_3OH clump found by Pratap et al. (1999). Particularly, the SiO map shows a second peak close to the estimated position of the CH_3OH outflow centre found by Pratap et al. (1999). As expected, in both sources the region of the HCO^+ absorption is coincident with the position of the 88 GHz continuum peak, as shown in Fig. 8: this proves that it is a *true* absorption feature, not a self-absorption effect.

Towards G29.96−0.02, the peak of the molecular emission is coincident with the core seen in the dust continuum and NH_3 emission by Cesaroni et al. (1994a). We note that in this source most of the 88 GHz continuum is due

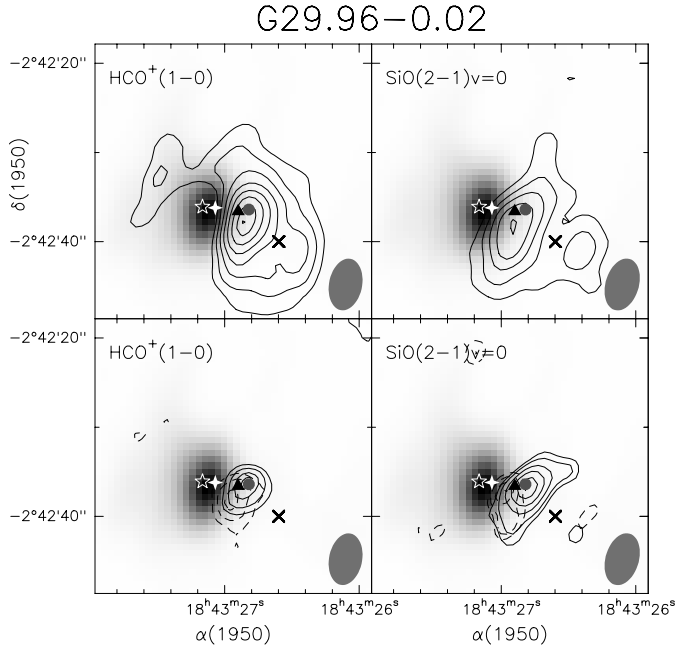


Fig. 6. Maps toward G29.96–0.02 in the $\text{HCO}^+(1-0)$ and $\text{SiO}(2-1) v=0$ emission averaged in velocity over all the line (top) and over the blue (solid contours) and red (dashed contours) wings (bottom), superimposed to the 88 GHz continuum map (grey scale). The ranges of velocity used in the maps are: for the HCO^+ 84–111 km/s for all the line, 84–89 km/s for the blue wing and 106–111 km/s for the red wing; for the SiO 85–111 km/s for all the line, 85–92 km/s for the blue wing and 104–111 km/s for the red wing. The contour levels for the HCO^+ line are: –0.10, 0.10, 0.15, 0.20, 0.25, 0.3, 0.35, 0.4, 0.43 Jy/beam; –0.09, 0.09, 0.12, 0.15, 0.17 Jy/beam (blue) and –0.09, 0.09, 0.12, 0.15 Jy/beam (red). The contour levels for the SiO are: –0.05, 0.05, 0.10, 0.15, 0.20, 0.25 Jy/beam; –0.09, –0.07, 0.07, 0.09, 0.12, 0.15, 0.18, 0.20 Jy/beam (blue) and –0.09, –0.07, 0.07, 0.09, 0.12, 0.145 Jy/beam (red). The star marks the position of the UC H II region ionizing star, the circle is the 88 GHz *dust* peak, the filled diamond the 24 GHz continuum peak, the triangle the $\text{NH}_3(4,4)$ HC peak, and the cross marks the peak position of the CH_3OH clump detected by Pratap et al. (1999).

to the free-free emission from the UC H II region, which is slightly displaced from the dust core (see Sect. 2.1). The lack of HCO^+ emission towards the UC H II peak is due to the absorption (see Fig. 8). The red and blue-shifted wing emissions of both HCO^+ and SiO appear only slightly separated along a E-W axis, parallel to that defined by the velocity gradient of the ammonia core (Cesaroni et al. 1998).

Towards G31.41+0.31, the peak of the HCO^+ and SiO clump is shifted southwards with respect to the position of the core traced by the dust emission and high excitation NH_3 and CH_3CN transitions (Cesaroni et al. 1998; Cesaroni et al. 1994b). In the case of HCO^+ , this is proba-

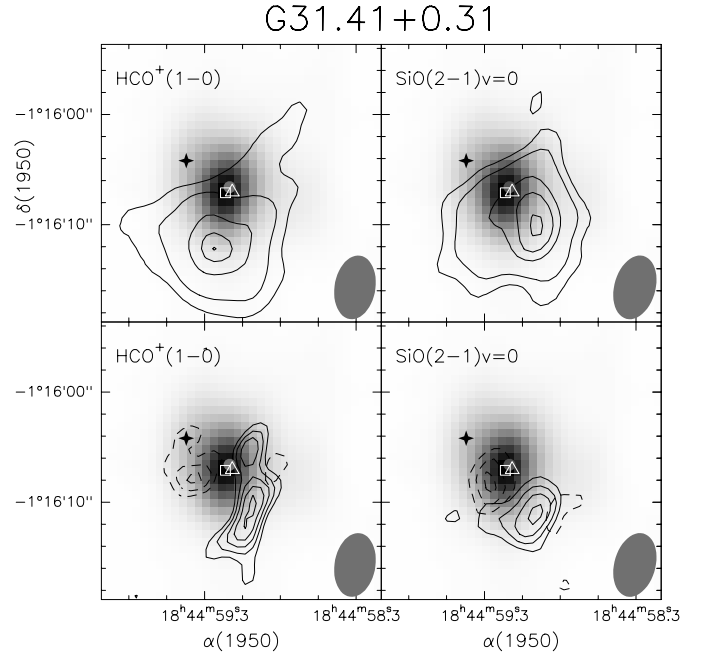


Fig. 7. Maps toward G31.41+0.31 in the $\text{HCO}^+(1-0)$ and $\text{SiO}(2-1) v=0$ emission averaged in velocity over all the line (top) and over the blue (solid contours) and red (dashed contours) wings (bottom), superimposed to the 88 GHz continuum map (grey scale). The ranges of velocity used in the maps are: for the HCO^+ 84–111 km/s for all the line, 84–89 km/s for the blue wing and 106–111 km/s for the red wing; for the SiO 83–111 km/s for all the line, 83–89 km/s for the blue wing and 106–111 km/s for the red wing. The contour levels for the HCO^+ line are: –0.05, 0.05, 0.10, 0.20, 0.25, 0.27 Jy/beam; –0.08, 0.08, 0.10, 0.12, 0.14, 0.16 Jy/beam (blue) and –0.08, 0.08, 0.10, 0.12 Jy/beam (red). The contour levels for the SiO are: –0.05, 0.05, 0.08, 0.12, 0.16, 0.20, 0.24 Jy/beam; –0.09, 0.09, 0.12, 0.15, 0.18 Jy/beam (blue) and –0.09, 0.09, 0.12, 0.14 Jy/beam (red). The square marks the position of the 110 GHz continuum peak, the circle is the 88 GHz *dust* peak, the filled diamond the 24 GHz continuum peak and the triangle the $\text{NH}_3(4,4)$ peak.

bly due to the fact that the core is coincident with the continuum peak, where the line is in absorption (see Fig. 8). In this case, the red and blue wings are clearly separated along a NE-SW axis, parallel to the velocity gradient seen in NH_3 and CH_3CN . The SiO red wing overlaps with the position of the dust continuum emission.

In Table 4 we report the parameters of the HCO^+ line emission. For each source we report the position, velocity, and synthesised beam brightness temperature (T_{SB}) for the emission and absorption peaks. In the same table we also report the observed ($\Theta_{3\sigma}$) and deconvolved ($\theta_{3\sigma}$) angular diameter of the HCO^+ molecular clump, computed from the 3σ contour, as explained in Sect. 3.1, and the deconvolved radius ($r_{3\sigma}$). In Table 5 we report the parameters for the SiO transition: position, velocity, and synthesised beam brightness temperature (T_{SB}) for the emission

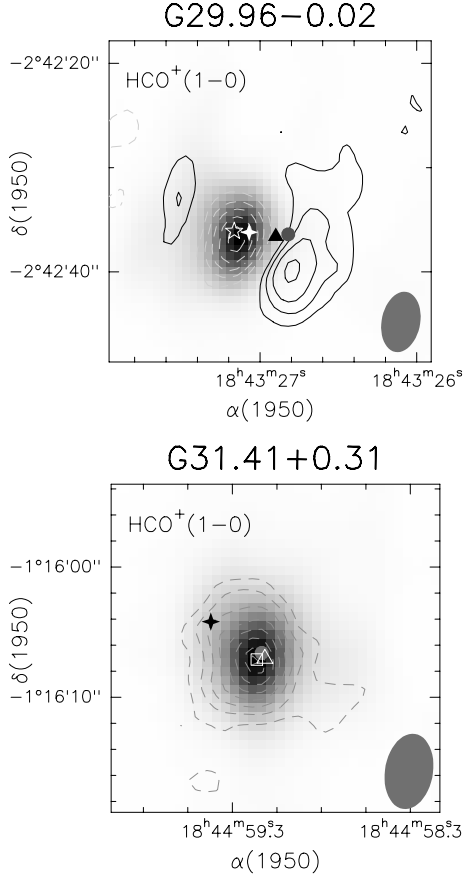


Fig. 8. Contour plots of the $\text{HCO}^+(1-0)$ line averaged over the absorption velocity range, 99–102 km/s for G29.96−0.02 and 95–99 km/s for G31.41+0.31, marked by the dotted lines in Figs. 4 and 5, overlaid on the 88 GHz continuum emission. Negative contours are dashed. The contour levels are −0.5, −0.4, −0.3, −0.2, −0.1, 0.1, 0.15, 0.2, 0.25 Jy/beam for G29.96−0.02 and −0.42, −0.4, −0.35, −0.3, −0.254, −0.2, −0.15, −0.1 Jy/beam for G31.41+0.31. Symbols are as in Figs. 6 and 7.

peak. We also give the values of the integrated line emission ($\int T dV$) and the peak velocity (V_{LSR}) from gaussian fits to the spectra obtained by averaging in each spectral channel the line emission within the contour corresponding to 50% of the peak in Figs. 6 and 7. The observed and deconvolved angular size corresponding to these contours and the deconvolved linear radius are also reported in Table 5.

4. Discussion

4.1. Mass estimates

Assuming optically thin dust thermal emission at 88 GHz, we calculated the mass of the millimeter continuum sources using: $M_d = \frac{F_\nu d^2}{\kappa_\nu B_\nu(T)}$, where F_ν is the observed integrated flux density on dust emission map (i.e. after subtracting the computed free-free emission), d the distance from the Sun, $B_\nu(T)$ the Planck function at the

assumed dust temperature T , $\kappa_\nu = \kappa_{230 \text{ GHz}} \left(\frac{\nu}{230 \text{ GHz}} \right)^\beta$ is the dust opacity per gram with $\kappa_{230 \text{ GHz}} = 0.005 \text{ cm}^2 \text{ g}^{-1}$, assuming a gas-to-dust ratio of 100 by mass (Preibisch et al. 1993), and β is taken from Table 1.

The gas kinetic temperatures of the two HCs have been estimated by Cesaroni et al. (1994a) using the $\text{NH}_3(4,4)$ line; they found 83 K for G29.96−0.02 and 120 K for G31.41+0.31. This latter value is consistent with the estimate of 123 K based on the CH_3CN observations by Cesaroni et al. (1994b). We used the temperature derived from the hot molecular gas, rather than the lower temperature derived from the global SED fit, because the latter is an estimate of the extended envelope temperature. In fact, the temperature is determined by the grey-body spectrum peak, i.e. the IRAS flux values, which are sensitive to the extended dust emission, while the continuum emission detected in our 88 GHz maps is dominated by the hot dust within the HC. With these temperatures, we estimated the mass of the hot core responsible for the 88 GHz dust continuum emission: $2900 M_\odot$ for G29.96−0.02 and $1500 M_\odot$ for G31.41+0.31. The latter is consistent with the estimate obtained from the 233 GHz flux for the same source ($1200 M_\odot$). While, for G29.96−0.02 due to the problems discussed in Sect. 2.1, the 233 GHz map cannot be used to derive a mass estimate.

The total mass of the molecular clumps surrounding the UC H II and HC can be estimated from the HCO^+ and SiO transitions. Here we will attempt to evaluate the masses using the virial and LTE assumptions. Given the velocity structures and complex line shapes observed in both lines, these estimates are affected by large uncertainties.

Assuming that the $\text{HCO}^+(1-0)$ is optically thick, the peak T_{SB} (Table 4) can be used as an estimate of the gas kinetic temperature. Another estimate of the temperature of the molecular clump as a whole can be obtained from the continuum SED fits presented in Sect. 3.1. These two estimates are consistent for G29.96−0.02, while for G31.41+0.31 the HCO^+ estimate is much lower. This discrepancy probably arises from the fact that in this source the absorption occurs towards the molecular clump peak, while in G29.96−0.02 the molecular clump, centered on the HC, is shifted from the position of the UC H II where the absorption is centered. We decided to adopt an average value of 30 K for both clumps. We assumed an SiO abundance of 7×10^{-11} with respect to H_2 , following the average value found by Codella et al. (1999) for the quiescent SiO component in a sample of young stellar objects. This value is also in agreement with the abundance derived by McMullin et al. (2000) for the quiescent gas in the Serpens core. Using the integrated line emission given in Table 5, we obtained a mass of $1600 M_\odot$ for G29.96−0.02 and $3200 M_\odot$ for G31.41+0.31. The main uncertainties in these estimates are the assumed SiO abundance and LTE-equilibrium condition; in fact the SiO molecule abundance is well known to be enhanced by a factor 10–100 in shocked regions (Bachiller & Pérez Gutiérrez 1997;

Table 4. Parameters of the $\text{HCO}^+(1-0)$ line emission and absorption

source		α_{1950}	δ_{1950}	V_{LSR} (km s^{-1})	T_{SB} (K)	$\Theta_{3\sigma}$ ($''$)	$\theta_{3\sigma}$ ($''$)	$r_{3\sigma}$ (pc)
G29.96−0.02	emission	18:43:26.87	−2:42:37.8	95.5	25.7	15.3	14.6	0.21
	absorption	18:43:27.15	−2:42:37.1	98.8	−6.0			
G31.41+0.31	emission	18:44:59.15	−1:16:11.5	92.1	17.2	14.4	13.7	0.26
	absorption	18:44:59.15	−1:16:07.3	97.2	−5.1			

Table 5. Parameters of the $\text{SiO}(2-1)$ $v=0$ line emission

source	α_{1950}	δ_{1950}	T_{SB} (K)	$\int T dV$ (K km s^{-1})	V_{LSR} (km s^{-1})	ΔV_{FWHM} (km s^{-1})	$\Theta_{50\%}$ ($''$)	$\theta_{50\%}$ ($''$)	$r_{50\%}$ (pc)
G29.96−0.02	18:43:26.91	−2:42:39.2	8.1	39.3	97.9	10.5	7.7	6.1	0.09
G31.41+0.31	18:44:58.96	−1:16:10.8	6.6	39.8	95.7	15.3	8.6	7.2	0.14

Codella et al. 1999). Such abundance enhancement would lead to unrealistically high mass estimates, unless the SiO is confined to an outflow.

To derive the virial mass from the $\text{SiO}(2-1)$ $v=0$ transition we used the FWHM calculated from the gaussian fit (Sect. 3.2, Table 5). We estimated a mass of $2500 M_{\odot}$ for G29.96−0.02 and $8000 M_{\odot}$ for G31.41+0.31. Owing to the fact that the SiO emission might arise from outflowing gas, which would increase the line FWHM, these values should be considered as upper limits. In the case of $\text{HCO}^+(1-0)$, the presence of the absorption feature makes very difficult to determine the intrinsic FWHM of the line. We fitted the line profile with two gaussian components, one in emission and one in absorption. The resulting linewidths of the emission component are 6.1 and 7.2 km s^{-1} for G29.96−0.02 and G31.41+0.31, respectively. The resulting virial mass estimates, using the sizes from Table 4, are 2000 and $3400 M_{\odot}$ for G29.96−0.02 and G31.41+0.31, respectively. However, the fit is strongly biased by the line wings and thus the resulting virial mass is most probably overestimated. This problem is particularly evident in G31.41+0.31, where these features are detected in both SiO and HCO^+ , and the virial mass estimates are less reliable and a few times higher than the masses derived from the dust emission or using the LTE approximation.

In conclusion, considering all the uncertainties in each of the methods discussed above, our estimates of the masses of the molecular clumps in both sources are consistent with $2000 M_{\odot}$ with an error of $\sim 50\%$.

4.2. Gas kinematics

We investigated the presence of a velocity gradient along the axes parallel and perpendicular to the direction where such a gradient was found in the $\text{NH}_3(4,4)$ (Cesaroni et al. 1998) and $\text{CH}_3\text{CN}(6-5)$ transitions (Cesaroni et al. 1994b; Olmi et al. 1996). For both the $\text{HCO}^+(1-0)$

and $\text{SiO}(2-1)$ $v=0$ lines we averaged the emission along the axis from the UC H II region peak to the core, and perpendicularly to it. This axis is along the E-W direction for G29.96−0.02 and along the NE-SW direction for G31.41+0.31. In Figs. 9 and 12 the position-velocity diagrams are shown, respectively for G29.96−0.02 and G31.41+0.31: we plotted, in the top panles for $\text{HCO}^+(1-0)$ and in the bottom for $\text{SiO}(2-1)$ $v=0$, the offset along the axes previously described. In SiO a velocity-position trend is clearly seen along the “parallel” axes. The V_{LSR} varies from 89 to 107 km s^{-1} over $\sim 3''$ toward G29.96−0.02 and from 86 to 106 km s^{-1} over $\sim 4''$ toward G31.41+0.31. The corresponding velocity gradients are approximately $6 \text{ km s}^{-1} \text{ arcsec}^{-1}$ toward G29.96−0.02 and $5 \text{ km s}^{-1} \text{ arcsec}^{-1}$ toward G31.41+0.31, consistent with the velocity gradient of approximately $2 - 3 \text{ km s}^{-1} \text{ arcsec}^{-1}$ over $3''$ found along the same directions in ammonia by Cesaroni et al. (1998). A velocity gradient of the same order is seen in HCO^+ toward G31.41+0.31, while it is not evident in the case of G29.96−0.02, most likely because of the presence of absorption. In the following we propose an interpretation of these findings

4.2.1. G29.96−0.02

In the case of the G29.96−0.02 molecular clump, as shown in the position-velocity diagrams (Fig. 9), the center of the HCO^+ clump is coincident in both position and velocity with the NH_3 HC; which in turn is located at the geometrical center of the molecular clump, as shown in Fig. 1 of Kurtz et al. (2000). The HCO^+ absorption appears redshifted with respect to the molecular clump systemic V_{LSR} (as traced by C^{34}S and C^{17}O ; Cesaroni et al. 1991, Hofner et al. 2000), and positionally coincident with the UC H II region, located east of the emission geometrical center. HCO^+ channel maps in Fig. 10 also show blueshifted gas

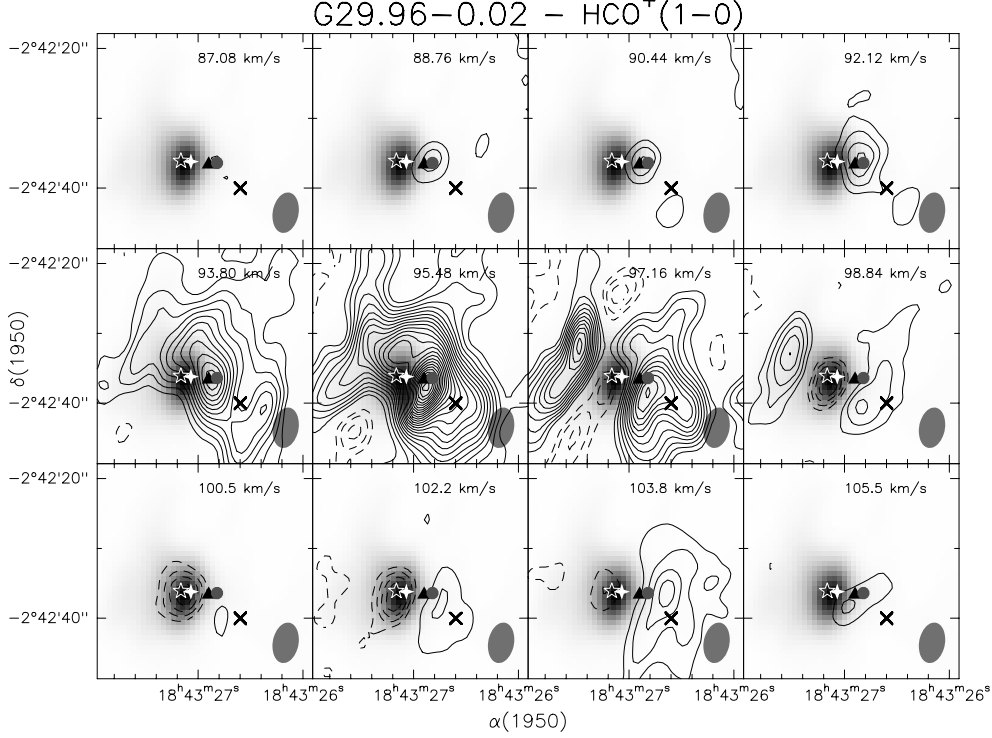


Fig. 10. Channel maps of $\text{HCO}^+(1-0)$ line towards G29.96–0.02, overlaid on the 88 GHz continuum emission. Contour levels are from -0.55 to -0.15 and from 0.15 to 2.45 by 0.1 Jy/beam. Negative contours are dashed. Symbols are as in Fig. 6.

emission toward the same direction, suggesting that the gas behind the H II region is moving towards the observer. This implies that the absorbing gas is moving along the line of sight towards the UC H II region. Both pv-diagrams also show that the maximum line-of-sight gas velocities are in the direction of the core position.

All these features can be easily interpreted if the UC H II is embedded within an infalling, spherically symmetric HCO^+ clump centered on the HC position. As shown in the sketch in Fig. 11, if the clump is contracting toward the NH_3 HC, toward the UC H II we will observe redshifted absorption from the gas in front of it and blueshifted emission from the gas behind it. At the position of the HC, there is emission at the highest line of sight velocities for both the redshifted and blueshifted gas.

The less abundant, optically thin SiO molecule traces a more internal region of the molecular clump. For this molecule, the pv-diagrams show a peak coincident with the HC, within the uncertainties, and a velocity structure consistent with that derived from the $\text{NH}_3(4,4)$ observations of Cesaroni et al. (1998). To explain this feature, we can hypothesize that SiO could trace the outer regions of the rotating $\text{NH}_3(4,4)$ disk or the inner regions of the infalling molecular clump (see Fig. 11). In the first scenario, the velocity gradient would be due to the velocity field in the outer regions of the disk. In this view the SiO abundance could be enhanced at the interface between the infalling molecular gas and the surface of the disk. Alternatively, the SiO emission could trace the innermost

and denser regions of the infalling envelope: the observed velocity gradient could then be produced by the asymmetric erosion by the UC H II. If the ionised gas is slightly off-center and further away from the observer with respect to the center of the infalling clump (as sketched in Fig. 11), blue-shifted SiO gas is eroded from one of the sides of the clump giving the illusion of a velocity gradient across the core. It should be noted, however, that the SiO is generally thought to trace outflowing material, as shown by several authors (Bachiller & Pérez Gutiérrez 1997; Cesaroni et al. 1999a; Acord et al. 1997), therefore one cannot exclude *a priori* the possibility that the velocity structure observed at the HC position (Fig. 6, bottom panels) may be due to a compact jet-outflow component unresolved by our observations.

At the position of the CH_3OH core detected by Pratap et al. (1999) we detect emission in both SiO and HCO^+ . We do not detect any clear signature of outflowing gas at that location, and favour the interpretation of a second, less massive molecular clump. Future higher resolution observations may allow to clarify the matter definitively.

4.2.2. G31.41+0.31

Compared to G29.96–0.02, the structure of G31.41+0.31 is more difficult to interpret. In this case, the bulk of the free-free emission from the UC H II region is along the same line of sight of the $\text{NH}_3(4,4)$ HC detected by Cesaroni et al. (1994a, 1998). Due to the absorption at the position

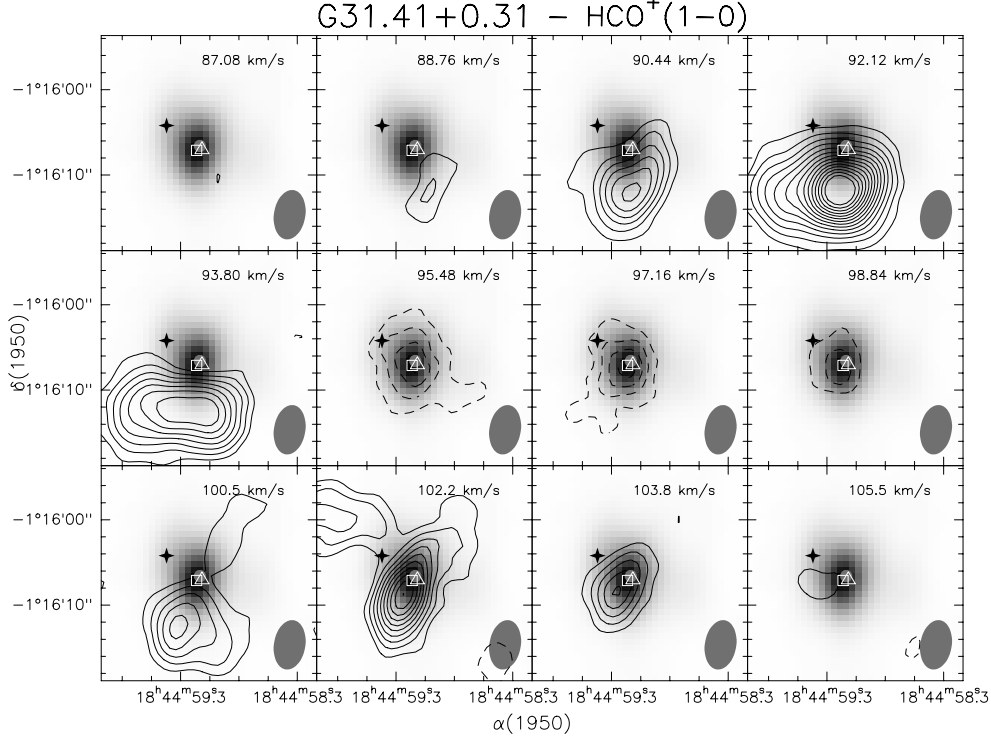


Fig. 13. As fig. 10 for G31.41+0.31. The contour levels are from -0.45 to -0.15 and from 0.15 to 1.65 by 0.1 Jy/beam. Symbols are as in Fig. 7

of the HC, the observed molecular line emission peak, both in HCO^+ and SiO , is south of the HC (Figs. 7 and 8).

The pv-diagrams (Fig. 12) show at high velocity, $V \geq 8$ km/s from the HC V_{LSR} , in both transitions, a gradient consistent with that observed in $\text{NH}_3(4,4)$ (Cesaroni et al. 1998). At lower velocity, however, the situation in HCO^+ is more complicated, with emission and absorption occurring toward the same line of sight at both blueshifted and redshifted velocities, with respect to the V_{LSR} of the HC and of the molecular clump as seen in C^{34}S and C^{17}O (Cesaroni et al. 1991; Hofner et al. 2000). The channel maps (Fig. 13) clearly show the superposition of these velocity features, and show an extension of the emission at blue velocities to the south of the HC position. In SiO , the emission peak lies south-west of the NH_3 HC and is blueshifted with respect to the latter (Figs. 7 and 12). The red emission (Fig. 7) peaks toward the HC, whereas the line bulk and the blue emission peak south-west of the HC, the velocity gradient agreeing with that seen in NH_3 .

It seems that there is a north-south gradient from red to blueshifted emission in HCO^+ , possibly tracing an outflow or the outer regions of the NH_3 disk, and a NE-SW gradient in SiO , compatible with the disk hypothesis. Thus, while the observed velocity field could also be interpreted as a combination of infall, outflow and rotation, as it may happen in similar regions (see e.g. Wilner et al. 1996), it is clear that we lack the spatial resolution required to properly separate the various components. In fact, at present we cannot exclude the possible alternative explanation that we are actually observing the superposi-

tion of two molecular cores, one located at the NH_3 HC position and the second south of it, where the HCO^+ and SiO emission peak. In this view, the velocity structure we observe would be partially produced by the superposition of the velocities of the two cores. However, we note that unlike G29.96–0.02, in G31.41+0.31 the absorption dip is seen at the centre of the HCO^+ line: this seems to be more consistent with the disk hypothesis, as collapse and outflow should determine a shift in velocity of such an absorption dip. In conclusion, we would tend to favour the disk hypothesis, although possibly in a more complex scenario involving outflow and/or infall.

5. Conclusions

Our interferometric observations show that the HCs and UC H II in G29.96–0.02 and G31.41+0.31 are embedded within massive gaseous clumps with a complex velocity structure. The masses of the clumps as derived from the millimeter continuum emission and from virial and LTE estimates based on the molecular line emission are in the range $1000\text{--}3000 M_{\odot}$ for both sources (with G31.41+0.31 being slightly more massive than G29.96–0.02). In G29.96–0.02 the HC is located close to the geometrical center of the clump and there is compelling evidence for a global motion of the molecular material onto the central object. In G31.41+0.31 our spatial resolution is not high enough to resolve the various components and it is not easy to disentangle the observed velocity structure. Most likely, in this source several kinematical components (outflow, rotation and possibly infall)

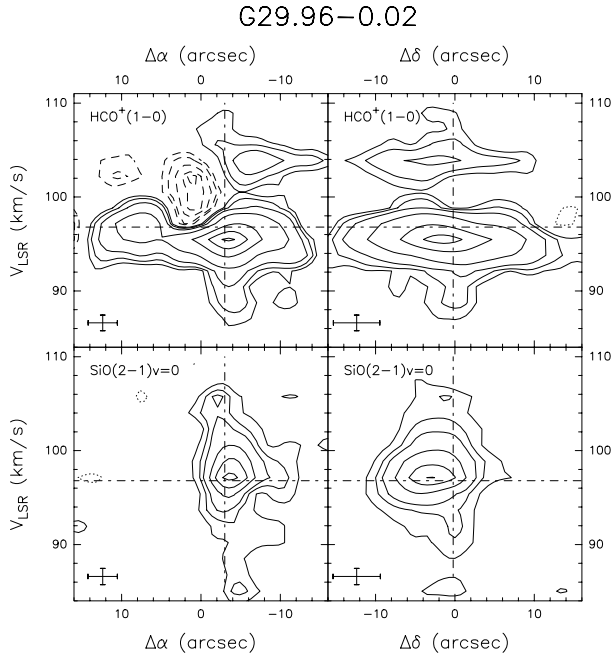


Fig. 9. Contour plots for G29.96−0.02 as a function of V_{LSR} and offset from the phase center along the E-W axis from the H II region and the core peak (left) and perpendicularly to it (right). The maps have been obtained by averaging the $\text{HCO}^+(1-0)$ (top) and $\text{SiO}(2-1) v=0$ (bottom) emission in G29.96−0.02 over $8''.4$ along the E-W axis and over $7''$ perpendicularly to it. The contour levels are: for HCO^+ , in $\Delta\alpha$ −0.4, −0.35, −0.25, −0.15, −0.09, 0.09, 0.15, 0.25, 0.50, 1.0, 1.5, 2.0 Jy/beam, in $\Delta\delta$ −0.09, 0.09, 0.15, 0.25, 0.50, 1.0, 1.5 Jy/beam; for SiO , in $\Delta\alpha$ −0.15, −0.09, 0.09, 0.15, 0.20, 0.30, 0.40, 0.50 Jy/beam, in $\Delta\delta$ −0.09, 0.09, 0.15, 0.20, 0.40, 0.49 Jy/beam. The dot-dashed lines mark the position and the velocity of the core detected in $\text{NH}_3(4,4)$ by Cesaroni et al. (1998).

are merged together by the spatial resolution of our observations.

In both regions our observations are consistent with earlier claims of the presence of rotating disks around young accreting massive (proto-)stars (Cesaroni et al. 1998). However, our spatial resolution does not allow us to definitely prove such claims and alternative models to interpret our observations are still viable. To definitely solve this dilemma and to probe the detailed structure of G31.41+0.31, higher resolution observations are needed.

Acknowledgements. The Owens Valley millimeter-wave array is supported by NSF grant AST-96-13717. Research at Owens Valley on the formation of young stars and planets is also supported by the *Norris Planetary Origins Project*. This work was partly supported by ASI grant ARS-98-116 to the Osservatorio di Arcetri.

References

Acord J.M., Walmsley C.M., Churchwell E., 1997, ApJ, 475, 693

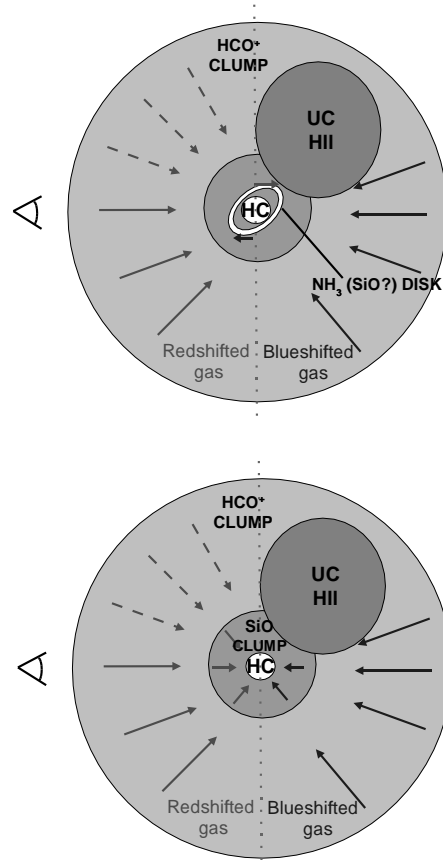


Fig. 11. Sketch of the infall model for G29.96−0.02. The SiO could trace the outer regions of the rotating $\text{NH}_3(4,4)$ disk (top) or the inner regions of the infalling molecular clump (bottom). Arrows show the gas velocity with respect to the clump V_{LSR} . The dashed arrows represent the gas seen in absorption toward the UC H II. The observer is on the left side.

- Afflerbach A., Churchwell E., Hofner P., Kurtz S., 1994, ApJ, 437, 697
 Bachiller R., Pérez Gutiérrez M., 1997, ApJ, 487, L93
 Ball R., Meixner M.M., Keto E., Arens J.F., Garrett Jernigan J., 1996, AJ, 112, 1645
 Cesaroni R., Felli M., Jenness T., Neri R., Olmi L., Robberto M., Testi L., Walmsley C.M., 1999a, A&A, 345, 949
 Cesaroni R., Felli M., Walmsley C.M., 1999b, A&AS, 136, 333
 Cesaroni R., Felli M., Testi L., Walmsley C.M., Olmi L., 1997, A&A, 325, 725
 Cesaroni R., Hofner P., Walmsley C.M., Churchwell E., 1998, A&A, 331, 709
 Cesaroni R., Walmsley C.M., Kömpe C., Churchwell E., 1991, A&A, 252, 278
 Cesaroni R., Churchwell E., Hofner P., Walmsley C.M., Kurtz S., 1994, A&A, 288, 903
 Cesaroni R., Olmi L., Walmsley C.M., Churchwell E., Hofner P., 1994, ApJ, 435, L137
 Chini R., Kreysser E., Mezger P.G., Gemünd H.-P., 1986, A&A, 154, L8
 Churchwell E., Walmsley C.M., Cesaroni R., 1990, A&AS, 83, 119

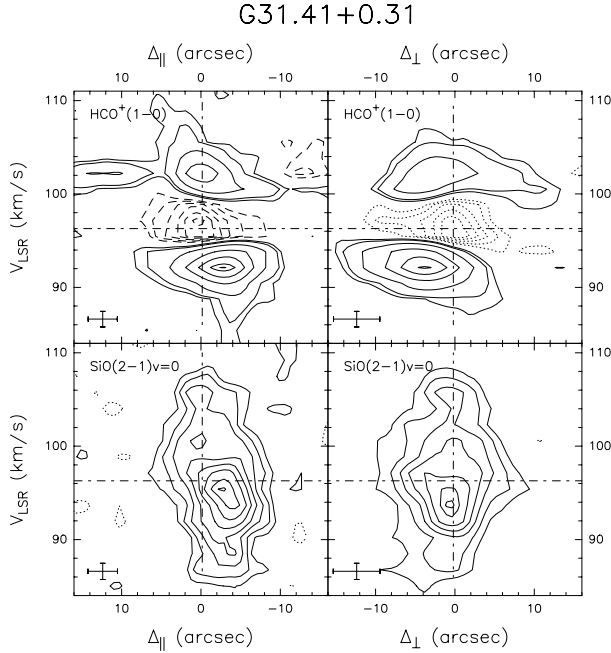


Fig. 12. Contour plots for G31.41+0.31 as a function of V_{LSR} and offset from the phase center along the SW-NE axis from the H II region and the core peak (left) and perpendicularly to it (right). The maps have been obtained by averaging the $\text{HCO}^+(1-0)$ (top) and $\text{SiO}(2-1) v=0$ (bottom) emission in G31.41+0.31 over $10''.5$ along the SW-NE axis and perpendicularly to it. The contour levels are: for HCO^+ , in $\Delta_{||}$ $-0.30, -0.25, -0.20, -0.15, -0.10, -0.06, 0.06, 0.10, 0.25, 0.50, 0.75, 1.0, 1.12$ Jy/beam, in Δ_{\perp} $-0.3, -0.25, -0.20, -0.15, -0.10, -0.06, 0.06, 0.10, 0.25, 0.50, 0.75, 1.0$ Jy/beam; for SiO , in $\Delta_{||}$ $-0.1, -0.06, 0.06, 0.10, 0.15, 0.20, 0.25, 0.30, 0.35, 0.38$ Jy/beam, in Δ_{\perp} $-0.09, -0.06, 0.06, 0.10, 0.15, 0.20, 0.25, 0.30, 0.32$ Jy/beam. The dot-dashed lines mark the position and the velocity of the core detected in $\text{NH}_3(4,4)$ by Cesaroni et al. (1998).

Codella C., Bachiller R., Reipurth B., 1999, *A&A*, 343, 585
 Condon J.J., Cotton W.D. et al., 1998, *AJ*, 115, 1693
 Fey A.L., Gaume R.A., Claussen M.J., Vrba F.J., 1995, *ApJ*, 453, 308
 Gaume R.A., & Mutel R.L., 1987, *ApJS*, 65, 193
 Herter T. et al., 1981, *ApJ*, 250, 186
 Hofner P., Churchwell E., 1996a, *A&AS*, 120, 283
 Hofner P., Kurtz S., Churchwell E., Walmsley C.M., Cesaroni R., 1996b, *ApJ*, 460, 359
 Hofner P., Kurtz S., Churchwell E., Watson A.M., 1996c, *BAAS*, 188, 17
 Hofner P., Wyrowski F., Walmsley C.M., Churchwell E., 2000, *ApJ*, 536, 393
 Hunter T.R., Phillips T.G., 1997, *ApJ*, 478, 283
 Kurtz S., Cesaroni R., Churchwell E., Hofner P., Walmsley C.M., 2000, in *Protostars & Planets IV*, ed. V. Mannings, A.P. Boss, & S.S. Russell (Tucson: Univ. Arizona Press), p. 299
 McMullin J.P., Mundy L.G., Blake G.A., Wilking B.A., Mangun J.G., Latter W.B., 2000, *ApJ*, 536, 845
 Molinari S., Brand J., Cesaroni R., Palla F., 1996, *A&A*, 308, 573

Molinari S., Testi L., Brand J., Cesaroni R., Palla F., 1998, *ApJ*, 505, L39
 Mooney T., Sievers A., Mezger P.G., Solomon P.M., Kreysa E., Haslam C.G.T., Lemke R., 1995, *A&A*, 299, 869
 Olmi L., Cesaroni R., Walmsley C.M., 1996, *A&A*, 315, 565
 Palla F. & Stahler S.W., 1993, *ApJ*, 418, 414
 Pratap P., Menten K.M., Snyder L.E., 1994, *ApJ*, 430, 129
 Pratap P., Megeath S.T., Bergin E.A., 1999, *ApJ*, 517, 799
 Preibisch Th., Osseukopf V., Yorke H.W., Henning Th., 1993, *A&A*, 279, 677
 Scoville N.Z., Carlstrom J.E., Chandler C.J., Phillips J.A., Scott S.L., Tilanus R.P.J., Wang Z., 1993, *PASP*, 105, 1482
 Testi L., Felli M., Persi P., Roth M., 1998, *A&A*, 329, 233
 Testi L., Hofner P., Kurtz S., Rupen M., 2000, *A&A*, 359, L5
 Tofani G., Felli M., Taylor G.B., Hunter T.R., 1995, *A&AS*, 112, 299
 Walsh A.J., Burton M.G., Hyland A.P., Robinson G., 1998, *MNRAS*, 301, 640
 Watson A.M., Hanson M.M., 1997, *ApJ*, 490, L165
 Watson A.M., Coil A.L., Shepherd D.S., Hofner P., Churchwell E., 1997, *ApJ*, 487, 818
 Wilner D.J., Ho P.T.P., Zhang Q., 1996, *ApJ*, 462, 339
 Wink J.E., Altenhoff W.J., Mezger P.G., 1982, *A&A*, 108, 227
 Wood D.O.S., Churchwell E., 1989a, *ApJ*, 340, 265
 Wood D.O.S., Churchwell E., 1989b, *ApJS*, 69, 831
 Wood D.O.S., Churchwell E., Salter C.J., 1988, *ApJ*, 325, 694